

Article

Open Access



# Photo-coupled electrocatalytic oxygen reduction to hydrogen peroxide using metal-free CNT-threaded oxidized g-C<sub>3</sub>N<sub>4</sub>

Qiong Zhu<sup>1</sup>, Jinchun Fan<sup>2,\*</sup> , Ying Tao<sup>1</sup>, Huan Shang<sup>2</sup>, Jingcheng Xu<sup>2</sup>, Dieqing Zhang<sup>1</sup>, Guisheng Li<sup>1,2,\*</sup> , Hexing Li<sup>1,\*</sup>

<sup>1</sup>The Education Ministry Key Lab of Resource Chemistry, Shanghai Key Laboratory of Rare Earth Functional Materials, Shanghai Normal University, Shanghai 200234, China.

<sup>2</sup>School of Materials and Chemistry, University of Shanghai for Science and Technology, Shanghai 200093, China.

**Correspondence to:** Dr. Jinchun Fan, School of Materials and Chemistry, University of Shanghai for Science and Technology, No. 516 Jungong Road, Yangpu District, Shanghai 200093, China. E-mail: jcfan@usst.edu.cn; Prof. Guisheng Li, School of Materials and Chemistry, University of Shanghai for Science and Technology, No. 516 Jungong Road, Yangpu District, Shanghai 200093, China. E-mail: liguisheng@usst.edu.cn; Prof. Hexing Li, The Education Ministry Key Lab of Resource Chemistry, Shanghai Key Laboratory of Rare Earth Functional Materials, Shanghai Normal University, No. 100 Guilin Road, Xuhui District, Shanghai 200234, China. E-mail: hexing-li@shnu.edu.cn

**How to cite this article:** Zhu Q, Fan J, Tao Y, Shang H, Xu J, Zhang D, Li G, Li H. Photo-coupled electrocatalytic oxygen reduction to hydrogen peroxide using metal-free CNT-threaded oxidized g-C<sub>3</sub>N<sub>4</sub>. *Energy Mater* 2022;2:200029. <https://dx.doi.org/10.20517/energymater.2022.33>

**Received:** 12 Jun 2022 **First Decision:** 8 Jul 2022 **Revised:** 16 Jul 2022 **Accepted:** 28 Jul 2022 **Published:** 10 Aug 2022

**Academic Editors:** Yuping Wu, Hao Liu **Copy Editor:** Tiantian Shi **Production Editor:** Tiantian Shi

## Abstract

Hydrogen peroxide (H<sub>2</sub>O<sub>2</sub>) has been widely used in environmental cleaning, hospital disinfecting and chemical engineering. Compared to the traditional anthraquinone oxidation method, the electrocatalytic two-electron oxygen reduction reaction (2e<sup>-</sup>ORR) to produce H<sub>2</sub>O<sub>2</sub> has become a promising alternative due to its green, safety and reliability. However, its industrial application is still limited by the slow reaction kinetics and low selectivity due to the competitive reaction of the 4e<sup>-</sup>ORR to H<sub>2</sub>O. Herein, we prepare a novel photoresponsive metal-free electrocatalyst based on oxidized g-C<sub>3</sub>N<sub>4</sub>/carbon nanotubes (OCN/CNTs) and introduce an external light field to realize the high-performance electrocatalytic 2e<sup>-</sup>ORR to produce H<sub>2</sub>O<sub>2</sub>. Impressively, the OCN/CNT electrocatalyst exhibits an outstanding H<sub>2</sub>O<sub>2</sub> productivity of 30.7 mmol/g<sub>cat</sub>/h with a high faradaic H<sub>2</sub>O<sub>2</sub> efficiency of 95%. The oxygen-containing groups of the OCN/CNTs promote the adsorption of oxygen intermediates and the photo-coupled electrocatalysis simultaneously improves the electron transport efficiency and enhances the electrocatalytic selectivity.



© The Author(s) 2022. **Open Access** This article is licensed under a Creative Commons Attribution 4.0 International License (<https://creativecommons.org/licenses/by/4.0/>), which permits unrestricted use, sharing, adaptation, distribution and reproduction in any medium or format, for any purpose, even commercially, as long as you give appropriate credit to the original author(s) and the source, provide a link to the Creative Commons license, and indicate if changes were made.



**Keywords:** Electrocatalytic oxygen reduction reaction (ORR), polymeric carbon nitride, carbon nanotubes, photo-coupled electrocatalysis, H<sub>2</sub>O<sub>2</sub> production

## INTRODUCTION

Hydrogen peroxide (H<sub>2</sub>O<sub>2</sub>) is a multifunctional strong oxidant that has been widely used in major industrial production, including chemical synthesis<sup>[1,2]</sup>, sterilization disinfection<sup>[3,4]</sup> and environmental governance<sup>[5,6]</sup>. H<sub>2</sub>O<sub>2</sub> is also regarded as a new clean fuel energy due to its extremely high transportation safety<sup>[7-10]</sup>. The traditional method of anthraquinone oxidation to produce H<sub>2</sub>O<sub>2</sub> requires high energy consumption and also causes serious pollution<sup>[11,12]</sup>. Recently, the electrocatalytic production of H<sub>2</sub>O<sub>2</sub> through the two-electron oxygen reduction reaction (2e<sup>-</sup>ORR) has arisen significant attention due to its safety, portability and environmental friendliness, which can effectively avoid the large-scale transportation of H<sub>2</sub>O<sub>2</sub> and realize its in-time production and use<sup>[13-15]</sup>. High-efficiency, low-cost electrocatalysts with excellent selectivity are pivotal for a high-performance electrocatalytic 2e<sup>-</sup>ORR to produce H<sub>2</sub>O<sub>2</sub>. Although traditional noble metal-based catalysts, including Pt, Au and their alloys, exhibit good electrocatalytic activity and 2e<sup>-</sup>ORR selectivity, their scarcity and high cost and the complexity of electrode forming strongly impede their practical applications<sup>[16,17]</sup>. Therefore, transitional metal-based and metal-free catalysts are constantly being designed and developed toward the electrocatalytic 2e<sup>-</sup>ORR and are close to the electrocatalytic performance of noble metal-based catalysts<sup>[18-21]</sup>.

Due to their high conductivity and structural tunability as metal-free catalysts, carbon-based 2e<sup>-</sup>ORR catalysts, including carbon nanotube (CNTs), graphene and carbon nanofibers, are regarded as the most promising potential alternatives to the abovementioned noble metal-based catalysts<sup>[22-25]</sup>. However, for pure carbon-based catalysts, their poor intrinsic catalytic activity cannot satisfy the demand for H<sub>2</sub>O<sub>2</sub> production. Furthermore, although the electrocatalytic activity and selectivity of carbon-based catalysts can be significantly improved by constructing structural defects<sup>[24,26]</sup> and doping with heteroatoms, such as N, B and O<sup>[22,27,28]</sup>, their catalytic performance is still relatively moderate with significant potential for improvement.

It is noteworthy that in addition to the modification of electrocatalysts, the introduction of external fields, including light, thermal, magnetic and piezoelectric fields, could further improve the catalytic performance<sup>[29-32]</sup>. Innovatively, Shen *et al.* found that Co<sub>3</sub>O<sub>4</sub> nanotube array-supported copper nanoparticles (NPs) showed a higher CO<sub>2</sub> conversion rate under illumination and demonstrated that the light field helped to reduce the potential barrier of electrocatalysis and promoted the electrode kinetics<sup>[33]</sup>. In general, when external light fields are introduced into traditional electrocatalysis, the specific electronic properties of the electrocatalyst, such as electron transfer, band bending, Fermi energy levels and intermediate desorption energy, are altered, which significantly changes the intrinsic path and performance of the catalysts<sup>[34-36]</sup>. More importantly, under the synergistic effect of photocatalysis and electrocatalysis, the use of a photo-coupled electrocatalytic system to enhance the 2e<sup>-</sup>ORR performance could be a promising strategy for H<sub>2</sub>O<sub>2</sub> production.

As a metal-free conjugated polymer, graphitic carbon nitride (g-C<sub>3</sub>N<sub>4</sub>) NPs have attracted significant attention in the application of the electrocatalytic ORR because of their unique three-dimensional morphology, tunable electronic structure, superior chemical stability, abundant pyridine nitrogen content, high durability and low cost<sup>[37-40]</sup>. More importantly, g-C<sub>3</sub>N<sub>4</sub> possesses a good adsorption capacity for oxygen due to its rich nitrogen content and has been successfully applied in the photocatalytic 2e<sup>-</sup>ORR to produce H<sub>2</sub>O<sub>2</sub><sup>[41-43]</sup>. Nevertheless, the poor H<sub>2</sub>O<sub>2</sub> selectivity and high electrical resistance result in inferior electrocatalytic H<sub>2</sub>O<sub>2</sub> production of the pristine g-C<sub>3</sub>N<sub>4</sub>. Various studies have shown that introducing a co-

catalyst and constructing a heterojunction system can significantly improve the charge migration and ORR performance of g-C<sub>3</sub>N<sub>4</sub><sup>[44-46]</sup>.

Herein, we propose a light-field enhancement route for improving the electrocatalytic 2e<sup>-</sup>ORR to produce H<sub>2</sub>O<sub>2</sub> by designing a novel photocoupled electrocatalyst based on oxidized g-C<sub>3</sub>N<sub>4</sub>/CNTs. Compared to standard electrocatalysis, photo-coupled electrocatalysis can reduce the electrode overpotentials, improve reaction kinetics and promote the electrode stability to facilitate catalytic performance. The CNTs can greatly promote the charge separation and light absorption of g-C<sub>3</sub>N<sub>4</sub> under the introduction of illumination, exposing more electrons for O<sub>2</sub> reduction. Furthermore, the g-C<sub>3</sub>N<sub>4</sub>/CNT hybrid is further oxidized to add more oxygen-containing groups. Rotating disk electrode (RDE) measurements and density functional theory (DFT) calculations illustrate that the combination of OCN and CNTs effectively improve the H<sub>2</sub>O<sub>2</sub> output and enhance the 2e<sup>-</sup>ORR selectivity.

## EXPERIMENTAL METHODS

### Preparation of OCN/CNTs

In a typical synthesis process, the GCN was obtained by 15 g of melamine calcined in a muffle furnace at 500 °C for 4 h at a heating rate of 2.19 °C/min. The CNT-threaded GCN-NPs were prepared by nitric acid oxidation. Firstly, the GCN nanorods (GCN-NRs) were synthesized by a hydrothermal treatment<sup>[47]</sup>. Specifically, 1.5 g of GCN and 1.5 g of urea were dissolved in 150 mL of deionized water and sonicated for 3 h until the solid matter was completely dispersed. Afterward, the solution mixture was transferred into a Teflon-stainless autoclave, followed by the synthetic reactions in an oven at 170 °C for 24 h. Subsequently, a certain amount of GCN-NRs ( $x = 100, 200, 300$  or 400 mg) and 1 mg of CNTs were dissolved in 200 mL of 12 M nitric acid in a three-neck round-bottom flask to synthesize the OCN- $x$ /CNTs ( $x = 100, 200, 300$  or 400 mg)<sup>[22]</sup>. The effect of different acidification times of the sample was subsequently investigated on the OCN-200/CNTs- $y$  ( $y = 0, 6, 12, 18$  or 24 h). The OCN/CNTs were collected by centrifuging in deionized water and ethanol several times until the pH of the solution reached neutral and dried overnight in a vacuum at 60 °C. The complementary information regarding the electrode preparation, characterization and photoelectric performance measurements of the electrodes, the detection of H<sub>2</sub>O<sub>2</sub> concentration, the RDE measurements and DFT calculation methods are given in the Supporting Information.

## RESULTS AND DISCUSSION

### Preparation of OCN/CNT catalysts

As shown in [Figure 1](#), the metal-free OCN/CNTs catalyst was synthesized via a three-step approach. In the first step, the bulk g-C<sub>3</sub>N<sub>4</sub> (B-GCN) was obtained by the high-temperature pyrolysis of melamine and was mainly composed of flake accumulation [[Supplementary Figure 1A and B](#)]. Next, through thermal polymerization, the B-GCN was rolled up and then formed into the GCN-NRs under the interaction between NH<sub>4</sub><sup>+</sup> and CO<sub>3</sub><sup>2-</sup> originating from urea<sup>[47]</sup>. Finally, the oxidized carbon nitride OCN/CNTs catalysts were prepared by nitric acid oxidation using the reflux condensation method<sup>[41]</sup>. It is noteworthy that the mass of the CNTs was fixed at 1.0 mg, the samples with different weights of g-C<sub>3</sub>N<sub>4</sub> were denoted as OCN- $x$ /CNTs ( $x = 100, 200, 300$  or 400 mg) and the samples with different oxidation times were labeled as OCN-200/CNTs- $y$  ( $y = 0, 6, 12, 18$  or 24 h). In the oxidation process, the GCN-NRs [[Supplementary Figure 1C and D](#)] were transformed into smaller-sized oxidized carbon nitride nanoparticles (OCN-NPs) [[Supplementary Figure 1E and F](#)] instead of bulk-OCN. The CNTs acted as building blocks for OCN/CNTs assembly. [Figure 2A and B](#) show the morphologies of the OCN/CNTs. From the inset of [Figure 2B](#), the mean size of the OCN-NPs was ~400 nm. The OCN-NPs and CNTs were assembled into OCN/CNTs hybrids through  $\pi$ - $\pi$  stacking. From TEM images [[Figure 2C and D](#)] of the OCN/CNTs, the CNTs were decorated on the surfaces of inner OCN microspheres with a size of ~5 nm. In addition, it could be seen

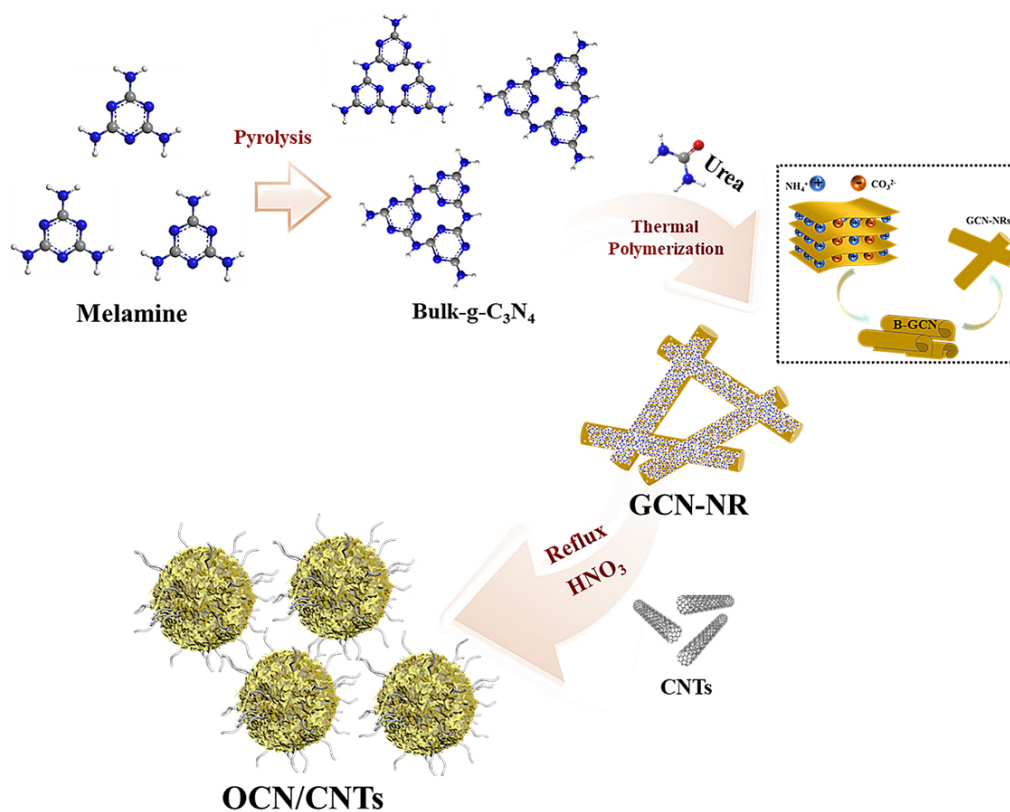


Figure 1. Synthetic process for metal-free OCN/CNTs.

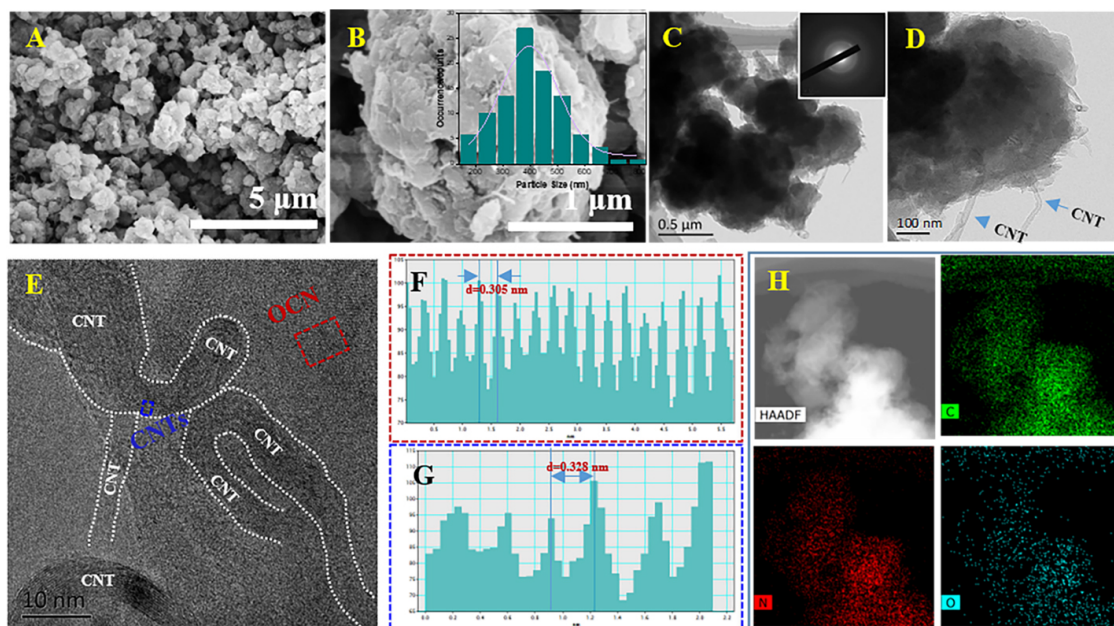


Figure 2. A-B: SEM images of OCN/CNTs (inset: corresponding size distribution histogram of OCN-NPs). C-D: TEM images of OCN/CNTs (inset: SAED image for OCN/CNTs). E: HRTEM image of OCN/CNTs. F-G: Lattice spacing for g-C<sub>3</sub>N<sub>4</sub> and CNTs. H: HAADF image of OCN/CNTs and corresponding EDS mapping images for C, N and O elements.

from the inset of [Figure 2C](#) that the composite sample presented a polycrystalline state. As shown in [Figure 2E](#), the CNTs were adsorbed on surfaces of OCN-NPs and in close contact with the CNTs, which could facilitate charge transfer. The CNTs show tube like-structure with distinct inner and outer walls. The *d*-spacings of 0.328 and 0.305 nm were attributed to the (002) diffraction crystal planes of graphitic carbon of CNTs [[Figure 2F](#)] and g-C<sub>3</sub>N<sub>4</sub> [[Figure 2G](#)], respectively. The high angle annular dark field (HAADF)-STEM and energy-dispersive X-ray spectroscopy (EDS) mapping images [[Figure 2H](#)] verified the presence and distribution of the main elements of C, N and O.

[Figure 3A](#) shows the X-ray diffraction (XRD) patterns of the OCN-NPs and OCN/CNTs hybrids with different weight ratios of OCN to CNTs. There were two characteristic diffraction peaks at  $2\theta$  of 13.1° and 27.6°, which were attributed to the (100) and (002) crystal planes of graphitic carbon nitride, respectively<sup>[42,43]</sup>. In the XRD patterns of OCN/CNTs hybrids, the (002) peak was slightly shifted accompanied with a decrease in intensity, because the CNTs were inserted between the layers of g-C<sub>3</sub>N<sub>4</sub> and the interlayers were loosened<sup>[48]</sup>. As the oxidation time increased, the intensity of the (002) diffraction peak decreased with the reduction of layer stacking [[Supplementary Figure 2A](#)]. The Raman spectra further confirmed the successful introduction of CNTs, with [Figure 3B](#) manifesting the D and G bands of g-C<sub>3</sub>N<sub>4</sub> located at 1316 and 1567 cm<sup>-1</sup>, respectively. As for OCN/CNTs, the D- and G-band peaks showed obvious spikes and migrated to 1330 and 1580 cm<sup>-1</sup> due to the interaction of g-C<sub>3</sub>N<sub>4</sub> and CNTs<sup>[27,49]</sup>. Furthermore, the G and D bands of the OCN-200/CNTs- $\gamma$  catalysts were not affected under the acidification, as indicated in [Supplementary Figure 2B](#). In the FTIR spectra of the OCN/CNTs, the vibration peaks of ~3430 and ~800 cm<sup>-1</sup> were indexed to the -OH and triazine units of the OCN/CNTs, respectively<sup>[50]</sup>. It is noteworthy that the intensity of the peak at ~3400–3500 cm<sup>-1</sup> increased with increasing acidification time, indicating that the increase in acidification time improved the degree of oxidation [[Supplementary Figure 3](#)].

X-ray photoelectron spectroscopy (XPS) was further conducted to characterize the composition of the OCN-200/CNTs-18h. From the full-scan XPS spectra, the C, N and O elements existed in the OCN-NPs and OCN-200/CNTs-18h catalysts [[Figure 3C](#)]. The C 1s spectrum of the OCN-NPs is shown in [Figure 3D](#). There were four peaks at 288.2, 285.87, 289.39 and 284.8 eV for the OCN-NPs, which were ascribed to the bonding of N=C-N, C-O, O-C=O and C-C/C=C, respectively<sup>[42,51,52]</sup>. After hybridizing with CNTs, the XPS peak of the N=C-N bond shifted to 288.9 eV, implying the  $\pi$ - $\pi$  conjugation between the CNTs and OCN-NPs. Interestingly, there were obvious increases in the intensity of the peaks for the C-O and O-C=O, indicating that the introduction of CNTs could enrich the oxygen-containing groups. The N 1s spectrum is shown in [Figure 3E](#), with the peaks at 399.59, 400.62 and 401.78 eV attributed to N<sub>2C</sub>, N<sub>3C</sub> and N-H<sub>x</sub>, respectively<sup>[43,44]</sup>. Similarly, from the O 1s XPS spectra [[Figure 3F](#)], the peak areas of C-O, C=O and O-H at 533.1, 532.5, and 531.8 eV became larger after incorporation with CNTs<sup>[48,50]</sup>. [Supplementary Figure 4](#) and [Supplementary Table 1](#) demonstrated that the increase in the acidification times could enhance the oxygen content of OCN/CNTs.

### Photo-coupled electrocatalytic oxygen reduction to H<sub>2</sub>O<sub>2</sub>

The photo-coupled electrocatalytic ORR installation diagram without any sacrificial agent is shown in [Figure 4A](#). From the UV-vis spectra [[Supplementary Figure 5](#)], it could be seen that the GCN could be regarded as an excellent photon absorber under light irradiation and the introduction of the CNTs enhanced the visible-light absorption. Thence, the photo-coupled electrocatalytic 2e<sup>-</sup>ORR performance of the different catalysts was estimated under visible-light illumination ( $\lambda \geq 400$  nm). From [Figure 4B](#), after applying the light field, the yield of H<sub>2</sub>O<sub>2</sub> and the faradaic H<sub>2</sub>O<sub>2</sub> efficiency were significantly improved compared to that of electrocatalysis. Obviously, photo-coupled electrocatalysis is an effective H<sub>2</sub>O<sub>2</sub> production strategy for oxygen reduction. Owing to the excellent photoelectrochemical property, the optimum yield of H<sub>2</sub>O<sub>2</sub> for the OCN/CNTs was 30.7 mmol/gcat/h after normalization, which was ~14 and

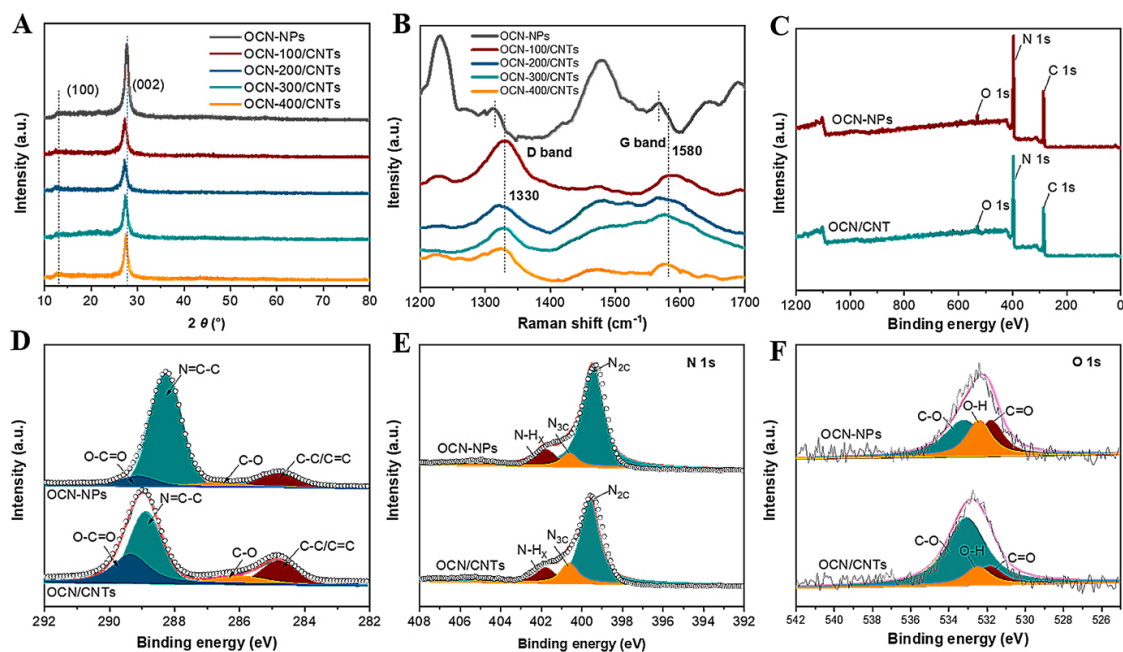


**Figure 3.** A: XRD patterns for all catalysts. B: Raman spectra for all catalysts. C: XPS survey spectra for OCN-NPs and OCN/CNTs. D-F: High-resolution XPS spectra of C 1s, N 1s and O 1s for OCN-NPs and OCN/CNTs.

~9 times higher than those of pristine g-C<sub>3</sub>N<sub>4</sub> and OCN-NPs, respectively.

The H<sub>2</sub>O<sub>2</sub> output of the catalysts is illustrated in Figure 4C, which demonstrates that the H<sub>2</sub>O<sub>2</sub> evolution rate has been significantly improved after incorporation with CNTs. The H<sub>2</sub>O<sub>2</sub> concentration for the OCN-400/CNTs was nearly four times higher than that of the OCN-NPs. The yield of H<sub>2</sub>O<sub>2</sub> also increased with increasing CNTs content of the OCN-100/CNTs. When the weight ratio of OCN-NPs to CNTs was 200:1, the H<sub>2</sub>O<sub>2</sub> concentration achieved the maximum. However, as the weight ratio of OCN-NPs to CNTs reached 100:1, the photo-induced electron used for the ORR would decrease due to the decrease in the relative content of OCN-NPs, resulting in a decrease in H<sub>2</sub>O<sub>2</sub> production. Subsequently, the effect of acidification time on the yield of H<sub>2</sub>O<sub>2</sub> with OCN/CNTs was also investigated in Supplementary Figure 6. The OCN-200/CNTs-18h with 18h of acidification time showed the best ORR activity for H<sub>2</sub>O<sub>2</sub> generation. This was mainly because the suitable amount of oxygen functional groups could improve the selectivity of H<sub>2</sub>O<sub>2</sub>, while too much oxygen content would reduce the conductivity of the catalyst, which was not conducive to producing H<sub>2</sub>O<sub>2</sub> [53]. Simultaneously, the yields of H<sub>2</sub>O<sub>2</sub> by using different catalyst samples were also affected by their different photoelectrochemical properties, which was confirmed in the subsequent photoelectrochemical measurements. Compared with the yield of H<sub>2</sub>O<sub>2</sub> of the pure OCN-NPs and OCNTs catalysts, the hybridization of OCN-NPs and CNTs greatly enhanced the efficiency of 2e<sup>-</sup>ORR to H<sub>2</sub>O<sub>2</sub> [Supplementary Figure 7]. The OCNTs almost has no light response, lacks electrons generated by light-excited semiconductors and could only accept electrons transmitted by external circuits, thus resulting in low H<sub>2</sub>O<sub>2</sub> production. To further study the interaction between the OCN and CNTs, the yields of H<sub>2</sub>O<sub>2</sub> for the OCN-bulk/CNTs and OCN/CNTs were obtained by mixing mechanically [Supplementary Figure 8].

The activity of the OCN/CNTs was superior to the OCN-bulk/CNTs and the mixture of OCN/CNTs, demonstrating that the  $\pi$ - $\pi$  conjugation between the OCN-NPs and CNTs in the OCN/CNTs greatly improved the efficiency of the separation and transmission of photogenerated carriers. Generally, the applied potential could affect the stability of the electrode and there would be a competing HER and 4e<sup>-</sup>ORR

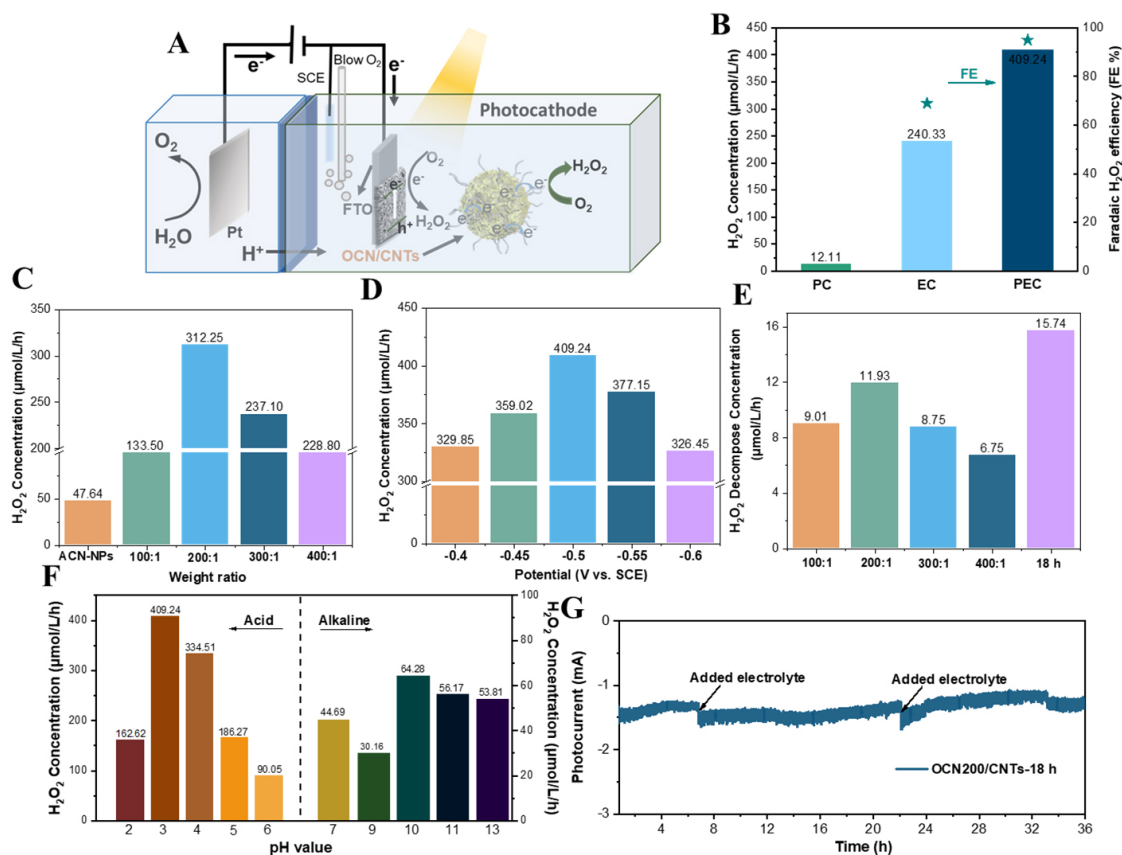


**Figure 4.** A: Schematic of the device for the photo-coupled electrocatalytic synthesis of H<sub>2</sub>O<sub>2</sub>. B: H<sub>2</sub>O<sub>2</sub> production of photocatalysis, electrocatalysis and photo-coupled electrocatalytic systems. C: H<sub>2</sub>O<sub>2</sub> production of OCN-x/CNTs (x = 100, 200, 300 or 400). D: Effect of bias voltage on H<sub>2</sub>O<sub>2</sub> production. E: Decomposition capacity of H<sub>2</sub>O<sub>2</sub> in different catalyst samples. F: Effect of different pH on H<sub>2</sub>O<sub>2</sub> production; G: Long-time photocurrent of H<sub>2</sub>O<sub>2</sub> production of the electrode. All the H<sub>2</sub>O<sub>2</sub> production experiments were under the conditions of pH = 3, V = -0.5 V vs. SCE and λ ≥ 400 nm.

[Equation (2)] in the applied potential<sup>[54,55]</sup>. Figure 4D shows that the optimal reaction voltage was -0.5 V vs. SCE, indicating that H<sub>2</sub>O<sub>2</sub> could be synthesized efficiently at low bias. Nevertheless, the inferior H<sub>2</sub>O<sub>2</sub> production [Supplementary Figure 9A] and the current [Supplementary Figure 9B] in the electrocatalytic system (-0.7 vs. SCE) were sufficient to reflect that the illumination could provide photogenerated electrons to promote the ORR to synthesize H<sub>2</sub>O<sub>2</sub> for the electrode and the advantages of high efficiency and energy saving in this system.



The decomposition rate of H<sub>2</sub>O<sub>2</sub> in the reaction process also played a very important role in the production of H<sub>2</sub>O<sub>2</sub>. The decomposition experiments of H<sub>2</sub>O<sub>2</sub> with different electrodes are presented in Figure 4E.

Compared to the high yield of  $\text{H}_2\text{O}_2$ , these decomposition amounts were negligible. It could be seen from Equation (2) that the pH value could greatly affect the performance of the ORR for producing  $\text{H}_2\text{O}_2$ . Figure 4F demonstrates that the OCN-200/CNTs-18h had extremely high photoelectrochemical activity at pH = 3 due to the high proton concentration. However, when the pH became acidic, the  $\text{H}_2\text{O}_2$  yield would be reduced mainly due to the competition of the HER from Equation (3)<sup>[48]</sup>. Furthermore, the yield of  $\text{H}_2\text{O}_2$  decreased as the pH increased from 3 to 7; however, it again increased at pH > 7, giving a peak at pH 10, before falling at a higher pH value. Surprisingly, the electrode achieved  $\text{H}_2\text{O}_2$  generation under alkaline conditions, which was mainly due to the peroxygen species produced by Equation (4) at high pH values<sup>[55]</sup>. The efficient generation of high-value clean energy ( $\text{H}_2\text{O}_2$ ) in a wide range of pH values could provide more possibilities for practical applications.

Supplementary Table 2 illustrates a comparison of the  $\text{H}_2\text{O}_2$  yield with current studies. The photocatalytic ORR to  $\text{H}_2\text{O}_2$  required the consumption of sacrificial agents and its activity was inferior. Compared to the electrocatalytic ORR<sup>[56,57]</sup>, the photo-coupled electrocatalytic system is relatively low in energy consumption and inexpensive. Our activity was higher than that of photocatalytic technology. For the electrode, the stability of the catalyst during the reaction process was extremely important<sup>[40,55]</sup>. In the follow-up experiment, we conducted a long-term reaction current test on the OCN-200/CNTs-18h electrode and found that the current remained unchanged after 36 h under the re-addition electrolyte [Figure 4G]. The faradaic  $\text{H}_2\text{O}_2$  efficiencies of OCN-NPs, OCN-200/CNTs-12h and OCN-200/CNTs-18h were 45.96%, 85.83% and 95.00%, respectively [Supplementary Figure 10A], indicating that the OCN-200/CNTs-18h was superior to the ORR to  $\text{H}_2\text{O}_2$ . From the evaluation of the cycle stability [Supplementary Figure 10B], the output of  $\text{H}_2\text{O}_2$  and the FE nearly remained the same in each cycle. The XRD and SEM analysis for the electrode before and after the reaction, also further demonstrated its excellent stability. XRD pattern analysis was carried out on the electrode after the reaction three times. Compared with pure FTO, the [002] crystal peak of  $g\text{-C}_3\text{N}_4$  appeared at  $27.6^\circ$  and the peak intensity remained unchanged compared with that before the reaction [Supplementary Figure 11A]. Moreover, the morphology of the catalyst did not change during the SEM analysis [Supplementary Figure 11B]. These results demonstrated that the designed OCN/CNTs electrode in this work had high activity and excellent stability.

### Photoelectrochemical properties of OCN/CNTs catalysts

The high charge separation efficiency and longer electron lifetime are beneficial to the improvement of the photoelectrochemical performance. For further understanding the mechanism for the high activity and stability of OCN/CNTs under illumination, the migration, transfer and recombination processes of the photogenerated electron-hole pairs in the OCN/CNTs electrodes were investigated. As shown in Figure 5A, the photocurrent densities for the OCN/CNTs with different ratios of OCN to CNTs under visible-light irradiation were much higher than that of OCN-NPs, demonstrating that the introduction of CNTs improves the charge migration significantly. More importantly, the OCN-200/CNTs show the highest photocurrent response with excellent carrier separation efficiency. In fact, a few OCN-NPs could reduce the quantity of photo-excited electrons, while redundant OCN-NPs would make electrons and holes easy to recombine<sup>[58]</sup>. The appropriate content of CNTs could effectively improve the conductivity of the OCN/CNTs and facilitate the transport of photogenerated carriers. From the electrochemical impedance spectroscopy (EIS) [Figure 5B], the OCN-200/CNTs possessed the smallest arc radius under low-frequency conditions, indicating the faster charge transfer process at the interface between the catalyst and the electrolyte. Similarly, the higher photocurrent signal [Figure 5C] and smaller arcs [Figure 5D] of OCN-200/CNTs-18h further provide powerful evidence that a suitable content of oxygen-containing groups could promote the separation of photo-induced electrons and separation in OCN/CNTs and then transfer faster to the electrolyte interface for the  $2e^-$  ORR to  $\text{H}_2\text{O}_2$ <sup>[3]</sup>.

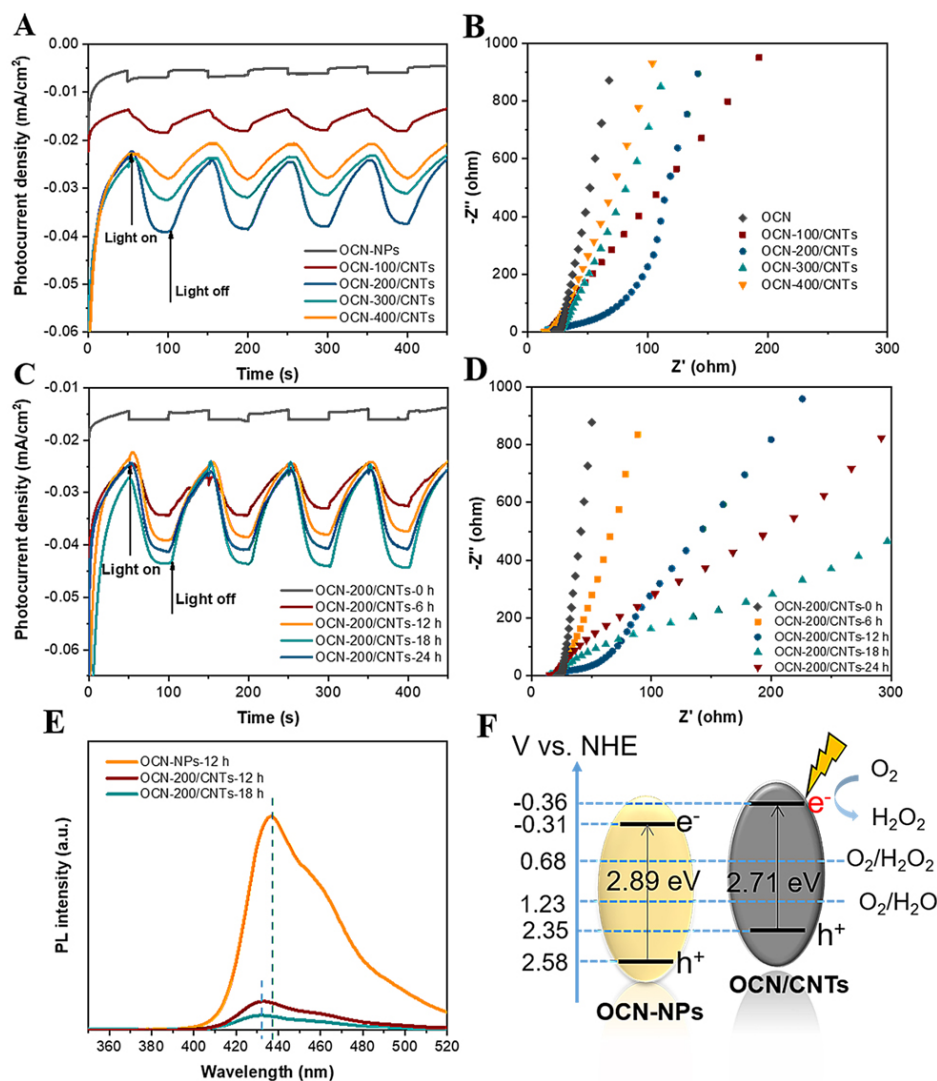


**Figure 5.** A: Photocurrent density of OCN-NPs and CNTs with different weight ratios ( $\lambda \geq 400$  nm,  $-0.5$  V vs. SCE). B: EIS Nyquist plots of OCN-NPs and CNTs with different weight ratios. C: Photocurrent density of OCN/CNTs with different acidification times ( $\lambda \geq 400$  nm,  $-0.5$  V vs. SCE). D: EIS Nyquist plots of OCN/CNTs with different acidification times. E: PL spectra of OCN-NPs, OCN-200/CNTs-12h and OCN-200/CNTs-18h. F: Band structure alignments of OCN-NPs and OCN-200/CNTs-18h.

In addition, photoluminescence (PL) spectra were employed to investigate the carrier separation processes of the photogenerated electron-hole pairs in the OCN/CNTs electrode. As shown in [Figure 5E](#), the main emission wavelength of OCN-NPs was located at 437 nm upon excitation at 325 nm. The emission wavelength of OCN/CNTs was 432 nm, slightly blue-shifted by 5 nm. The OCN-200/CNTs-18h showed the lowest PL intensity in comparison with those of the OCN-NPs, OCN-200/CNTs-12h and OCN-200/CNTs-18h, demonstrating the excellent efficient charge separation and fewer capture centers for the OCN-200/CNTs-18h. The Mott-Schottky plots [[Supplementary Figure 12](#)] were used to evaluate the flat band potential. The flat band potentials of the OCN-NPs and OCN-200/CNTs-18h were  $-0.40$  and  $-0.35$  eV, respectively. Generally, the conduction band position is  $0.1$  eV more negative than the flat band potential<sup>[5]</sup>. To illustrate the mechanism toward the ORR to H<sub>2</sub>O<sub>2</sub>, the electron band structures of the OCN-NPs and OCN-200/CNTs-18h are manifested in [Figure 5F](#). It could be seen that the CB of the OCN-200/CNTs-18h ( $-0.36$  eV) was more negative than that of the OCN-NPs ( $-0.31$  eV), indicating the OCN-200/CNTs-18h was

suitable for the  $2e^-$ ORR to  $H_2O_2$ . The bandgaps of the OCN-NPs and OCN-200/CNTs-18h were determined by the Kubelka-Munk function, corresponding to 2.89 and 2.71 eV, respectively [Supplementary Figure 13].

The relevant photoelectrochemical characterization under illumination and dark conditions was further used to understand the attribution of solar energy for the photo-coupled electrocatalytic performance. The smaller arcs and more negative current density of OCN-200/CNTs-18h in the EIS and LSV measurements [Figure 6A and B] verified that the introduction of illumination could improve the electron transfer efficiency and  $2e^-$ ORR performance. The corresponding lower Tafel plot slope [Figure 6C] under light indicated that solar energy could increase the kinetic rate of the reaction to promote the generation of  $H_2O_2$ . Furthermore, in the CV measurements in an oxygen atmosphere after 1000 cycles, the current density in dark conditions decreased and the half-wave potential decreased by 52 mV, while the current density increased slightly and the half-wave potential increased by 40 mV under illumination [Figure 6D], which was mainly because of the graphitic carbon nitride continuously producing photogenerated electrons for a supplement under the illumination, making the catalyst in a relatively stable state, while pure electrocatalytic technology was extremely unstable after 1000 cycles. The incident photon-to-current efficiency (IPCE) for the OCN/CNTs electrodes was measured to evaluate the quantum yield as a function of irradiation and displayed maximum efficiencies for OCN-200/CNTs-18h, OCN-200/CNTs-12h and OCN-NPs of 5.436%, 3.997% and 1.691%, respectively, at 360 nm [Supplementary Figure 14]. At 400 nm, the IPCE values of OCN-200/CNTs-18h, OCN-200/CNTs-12h and OCN-NPs were 2.175%, 1.479% and 0.518%, respectively. Compared with pure OCN-NPs and OCN-200/CNTs-12h, the introduction of appropriate CNTs and oxygen content could greatly promote the excellent photoelectric conversion efficiency and the utilization rate of solar energy. The electronic lifetimes ( $\tau$ ) determined from the Bode Plots are illustrated in Supplementary Figures 15 and 16. From Supplementary Table 3, compared to the OCN-NPs ( $\tau = 0.50$  s), the  $\tau$  of OCN-200/CNTs-18h increased to 1.31 s after incorporating with CNTs and oxygen-containing groups, demonstrating the introduction of CNTs and oxygen content significantly improved the electron migration efficiency, which promoted the  $2e^-$ ORR performance.

For the photo-coupled electrocatalytic system, the electrochemical activity surface area (ECSA) is an important indicator of catalytic performance since it could directly provide the surface area involved in the electrochemical reaction<sup>[59]</sup>. The double-layer capacitance ( $C_{dl}$ ) was measured from the cyclic voltammetry (CV) curves at different scan rates [Supplementary Figures 17 and 18]. The ECSA of the catalyst samples was calculated by  $ECSA = C_{dl}/0.0155 \text{ mF cm}^{-2}$ . After normalization, the ECSAs for the OCN-NPs, OCN-100/CNTs, OCN-200/CNTs, OCN-300/CNTs and OCN-400/CNTs were 0.14, 0.43, 0.67, 0.59 and 0.29  $\text{m}^2/\text{g}_{\text{cat}}$ , respectively [Figure 7A]. Figure 7B illustrates that the ECSAs of OCN-200/CNTs-18h and OCN-200/CNTs-12h were 0.74 and 0.67  $\text{m}^2/\text{g}_{\text{cat}}$ , respectively. Surprisingly, as determined from the  $N_2$  adsorption-desorption isotherms [Supplementary Figure 19 and Supplementary Table 4], the BET surface area of the OCN-NPs was higher than that of GCN and GCN-NRs, which may be due to the assemble of particles. Additionally, after combining with CNTs, the BET surface area of OCN/CNTs exhibited a slight decrease originating from blocking the pores of OCN-NPs. This demonstrated that the ECSA was more propitious to promote the photoelectrochemical activity of ORR to  $H_2O_2$  instead of the BET surface area. To further understand the selectivity of OCN-NPs and OCN-200/CNTs-18h for oxygen reduction reaction, the photoresponse of the OCN-NPs and OCN-200/CNTs-18h was carried out under an Ar and  $O_2$  atmosphere.

As shown in Figure 7C, whether in the Ar (inset) or  $O_2$  atmosphere, the photocurrent density of the OCN-200/CNTs-18h was always higher than that of the OCN-NPs, indicating the excellent carrier separation efficiency of the OCN-200/CNTs-18h catalyst. Interestingly, under the optimal reaction potential conditions ( $-0.5 \text{ V vs. SCE}$ ), the photocurrent response and current value of OCN-200/CNTs-18h were significantly

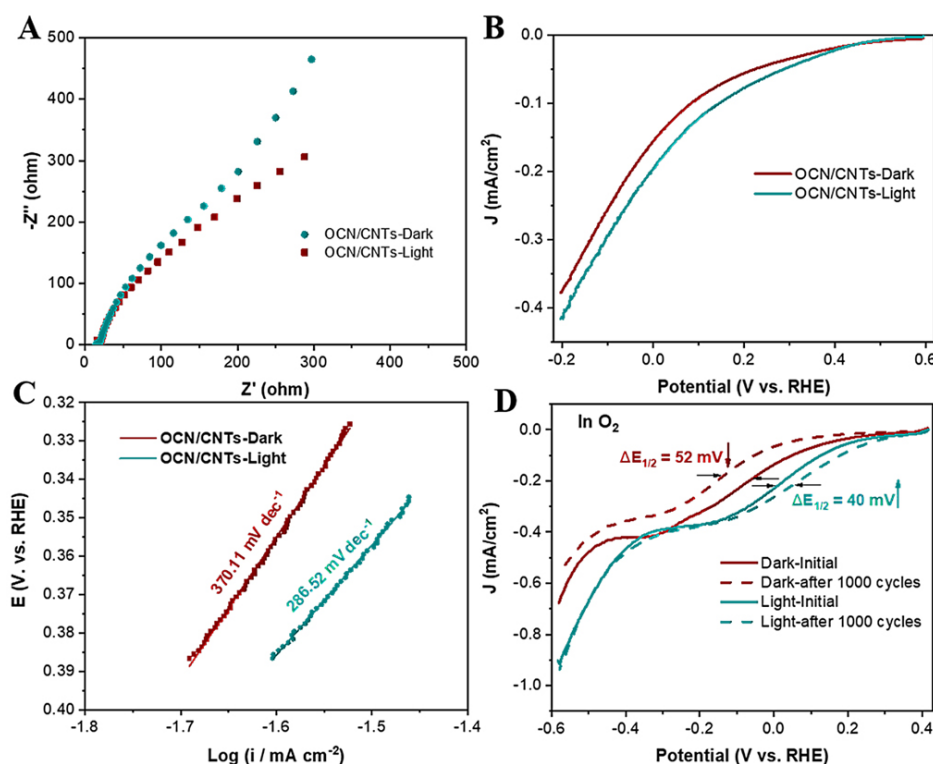


**Figure 6.** A: EIS and B: LSV measurements at 50 mV/s under light and dark for OCN-200/CNTs-18h. C: Corresponding Tafel plots. D: ORR polarization curves at 100 mV/s of OCN-200/CNTs-18h under light and dark before and after 1000 cycles in O<sub>2</sub>-saturated 0.5 M NaSO<sub>4</sub>.

enhanced in an O<sub>2</sub> atmosphere compared to in the Ar and air atmospheres [Figure 5C]. The linear sweep voltammetry (LSV) curves of the OCN-NPs and OCN-200/CNTs-18h under saturated Ar or O<sub>2</sub> atmospheres also confirmed the above-mentioned phenomenon [Figure 7D]. The OCN-200/CNTs-18h showed a more negative photocurrent under light and oxygen atmospheres than under dark and Ar atmospheres (inset). It is noteworthy that after illumination the current value of OCN-NPs and OCN/CNTs was lower than that under dark conditions and the Ar atmosphere. The same phenomenon occurred in the O<sub>2</sub> atmosphere of OCN-NPs, which was mainly caused by the increase in resistance after illumination<sup>[55]</sup>. This phenomenon highlighted that the OCN-200/CNTs-18h electrode was more conducive to electron transfer for the ORRs under the conditions of illumination and O<sub>2</sub> atmosphere. Both the photocurrent and LSV measurements in the Ar and O<sub>2</sub> atmospheres demonstrated that the electrode developed in this work with a superior selectivity for the ORR and could greatly inhibit the HER. Furthermore, the H<sub>2</sub>O<sub>2</sub> production under Ar and O<sub>2</sub> atmosphere is shown in Supplementary Figure 20, which demonstrates that the synthesized H<sub>2</sub>O<sub>2</sub> was derived from O<sub>2</sub>.

### Mechanism for 2e<sup>-</sup>ORR on OCN/CNTs

To further study the mechanism of the 2e<sup>-</sup>ORR on the OCN/CNT-based electrodes, the selectivity of the 2e<sup>-</sup>ORR was estimated by RDE measurements in 0.05 M Na<sub>2</sub>SO<sub>4</sub> electrolyte under an O<sub>2</sub> atmosphere. Based on the analysis for the effect of pH value on the H<sub>2</sub>O<sub>2</sub> production [Figure 3F], the pH value of electrolyte was adjusted to 3 for the RDE measurements with 1 M H<sub>2</sub>SO<sub>4</sub>. From the LSV curves of the catalysts under different rotation speeds [Figure 8A-C], the current density of the OCN-200/CNTs-18h was obviously superior to those of the OCN-NPs and OCN-200/CNTs-12h, suggesting that introducing CNTs and oxygen-containing groups improve the 2e<sup>-</sup>ORR electrocatalytic activity. The numbers of transferred

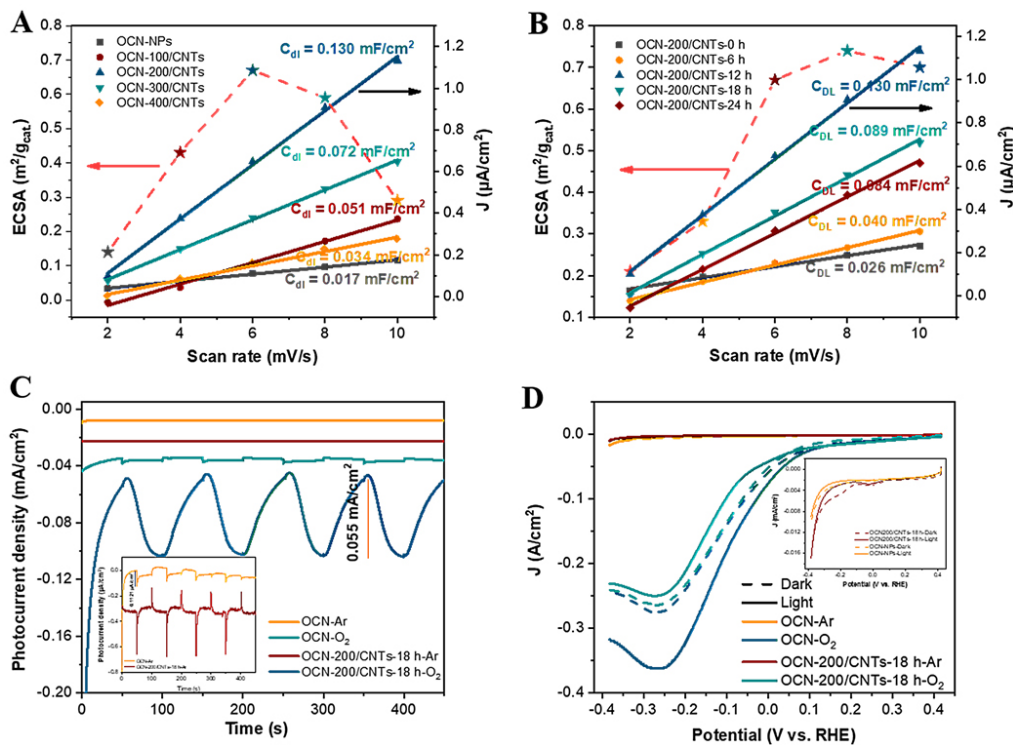


**Figure 7.** A-B:  $C_{dl}$  value calculated from CV curves and ECSA ( $m^2/g_{cat}$ ) for OCN-x/CNTs and OCN-200/CNTs-y. C: Photocurrent density of OCN-NPs and OCN/CNTs measured under a saturated Ar (inset) or  $O_2$  atmosphere and visible-light illumination ( $\lambda \geq 400$  nm,  $V = -0.5$  V vs. SCE); D: LSV of OCN-NPs and OCN/CNTs measured under a saturated Ar (inset) or  $O_2$  atmosphere with visible-light illumination ( $\lambda \geq 400$  nm, pH = 3).

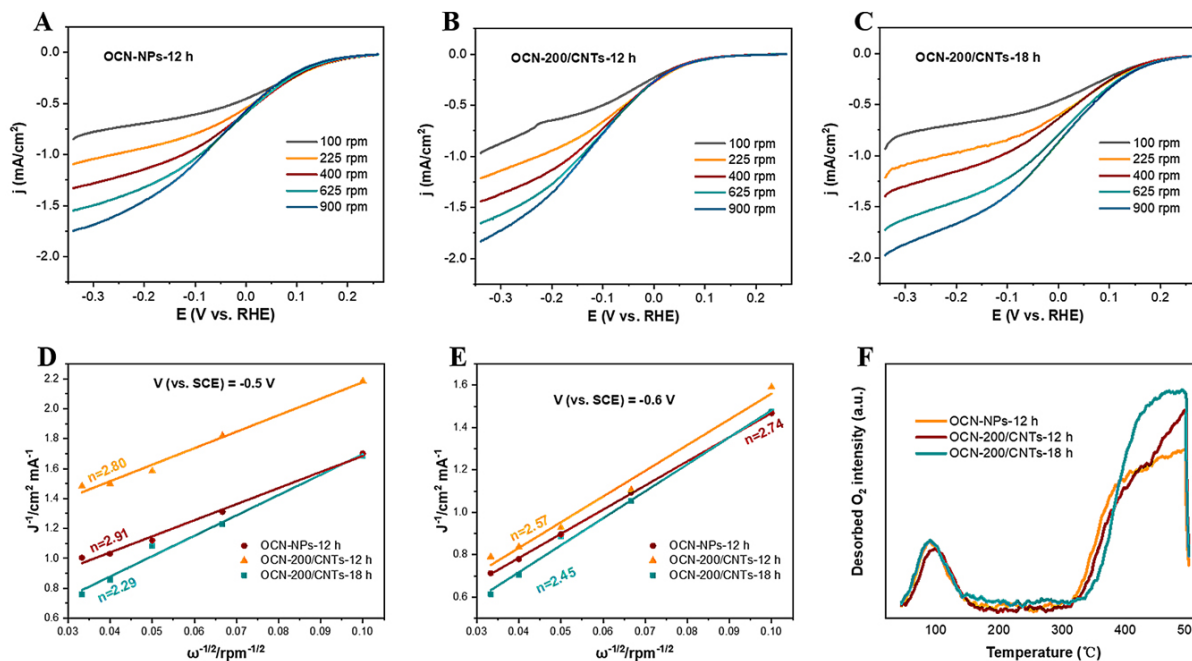


**Figure 8.** A-C: LSVs of OCN-NPs, OCN-200/CNTs-12h and OCN-200/CNTs-18h catalysts measured on a RDE at different rotating speeds with pH = 3 (scan rate 10 mV/s). D-E: Koutecky–Levich curves of OCN-NPs, OCN-200/CNTs-12h and OCN-200/CNTs-18h at -0.5 and -0.6 V vs. SCE. F: Comparison of TPD- $O_2$  among OCN-NPs, OCN-200/CNTs-12h and OCN-200/CNTs-18h.

electrons ( $n$ ) toward the ORR on the catalysts were determined by the Koutecky–Levich (K-L) equation [Equations (5) and (6)]:

$$j^{-1} = j_k^{-1} + b^{-1}\omega^{-1/2} \quad (5)$$

$$B = 0.2nF\nu^{-1/6} CD^{2/3} = A*n \quad (6)$$

where  $j$  is the measured current density,  $j_k$  is the kinetic current density,  $\omega$  is the rotating speed (rpm),  $F$  is the Faraday constant,  $\nu$  is the kinetic viscosity of water,  $C$  is the bulk concentration of  $O_2$  in water and  $D$  is the diffusion coefficient of  $O_2$ , respectively.

The contribution of all parameters (denoted as  $A = 0.032 \text{ mC S}^{-1/2}$ ) to Equation (6) were determined in a solution of  $Na_2SO_4$ <sup>[6]</sup>. The slope of the curve ( $B^{-1}$ ) calculated by linear regression for  $j^{-1}$  and  $\omega^{-1/2}$  at a designated voltage could determine the average number of electrons ( $n$ ) in the ORR. Figure 8D indicates that the measured  $n$  value of the OCN-NPs was 2.91, while the  $n$  values of OCN-200/CNTs-12h and OCN-200/CNTs-18h were 2.80 and 2.29 at the optimal reaction potential (-0.5 V vs. SCE), respectively. Similarly, the  $n_{\text{OCN-NPs}}$ ,  $n_{\text{OCN-200/CNTs-12h}}$  and  $n_{\text{OCN-200/CNTs-18h}}$  were 2.74, 2.57 and 2.45, respectively, at the reaction potential (-0.6 V vs. SCE) in Figure 8E. The results indicate that the appropriate introduction of CNTs and oxygen content were selective toward two-electron transfer to produce  $H_2O_2$ . Simultaneously, it also demonstrated that the photoelectrode of OCN-200/CNTs-18h with a superior selectivity of the two-electron pathway for ORR at a lower voltage, which was consistent with the  $H_2O_2$  production at the different potentials [Figure 3D]. To further demonstrate that the ORR procedure on the OCN-200/CNTs-18h was more inclined to the two-electron pathway, the temperature-programmed desorption (TPD) measure was used to study the adsorption capacity of  $O_2$  for the catalyst. In Figure 8F, the OCN-200/CNTs-18h shows an excellent chemisorption effect on  $O_2$  compared to the OCN-NPs and OCN-200/CNTs-12h, suggesting that the OCN-200/CNTs-18h could generate strong force to activate  $O_2$ . The adsorption capacities of  $O_2$  for the OCN/CNTs with different ratios of OCN to CNTs and acidification times were presented in Supplementary Figures 21 and 22, respectively. It could be seen that the appropriate amount of CNTs and oxygen content could improve the chemisorption of  $O_2$ .

DFT calculations were carried out to gain insights into the mechanism. The optimized structural models of the OCN-NPs and OCN-200/CNTs-18h are illustrated in Figure 9A and B, respectively. The CNTs interacted with the OCN-NPs via the  $\pi$ - $\pi$  conjugation. The relative Gibbs free energies of the reaction intermediates of the ORR to  $H_2O_2$  are shown in Figure 9C and D.  $O_2$  was adsorbed as an adsorption state ( $O_2^*$ ) on the catalyst surface, which was then converted to an intermediate state ( $OOH^*$ ) with free hydrogen in the aqueous solution. Subsequently, the intermediate state ( $OOH^*$ ) could undergo a proton coupling process with water molecules to form an adsorbed state  $HOOH^*$ , finally desorbing into  $H_2O_2$ <sup>[48,50]</sup>. In particular, the formation of the adsorption state ( $O_2^*$ ) on OCN-200/CNTs-18h was a spontaneous reaction corresponding to the  $\Delta G \sim -0.67$  eV. However, this process of OCN-NPs was a non-spontaneous process due to the endothermic  $\Delta G \sim 0.11$  eV and required a large activation energy barrier. This result indicated that the OCN-200/CNTs-18h electrode could thermodynamically preferentially facilitate the oxygen reduction to  $H_2O_2$  with a lower Gibbs free energy of adsorbed oxygen in comparison with OCN-NPs. The TPD confirmed the DFT results, as shown in Figure 8F, with OCN-200/CNTs-18h exhibiting excellent chemical adsorption properties of  $O_2$ . Based on the above experimental results, we believe that OCN-200/CNTs-18h is conducive to the two-electron ORR.

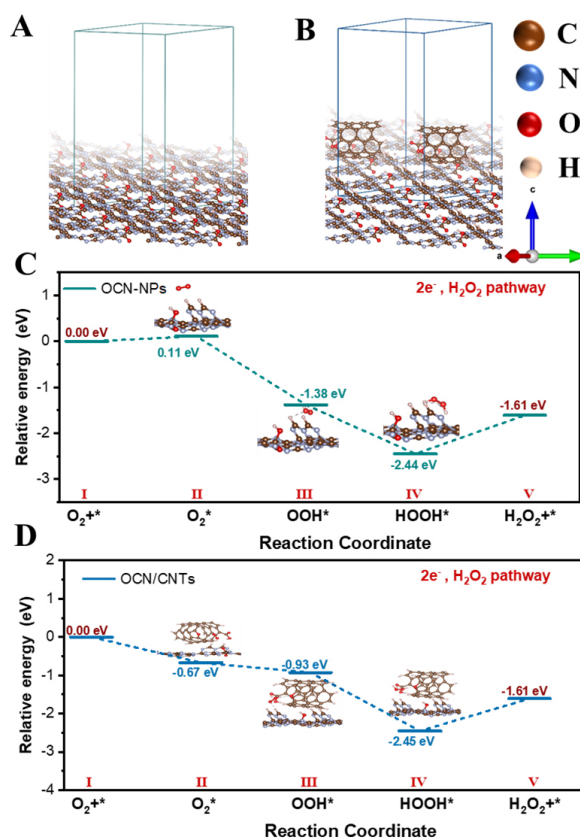


**Figure 9.** A-B: Optimized structures of OCN-NPs and OCN-200/CNTs-18h, respectively. C-D: Energy profiles of key possible ORR pathways on OCN-NPs and OCN-200/CNTs-18h, respectively.

## CONCLUSIONS

In summary, we developed a novel nanocomposite by threading OCN-NPs with CNTs through a controlled assembly. As an electrode material, it exhibited high efficiency in photo-coupled electrocatalytic H<sub>2</sub>O<sub>2</sub> production through the 2e<sup>-</sup>ORR with the optimum H<sub>2</sub>O<sub>2</sub> yield and faradaic H<sub>2</sub>O<sub>2</sub> efficiency reaching up to 30.7 mmol/g<sub>cat</sub>/h and 95%, respectively. Furthermore, it also displayed strong durability in a long reaction period. The high catalytic activity could be attributed to the unique structure of OCN/CNTs, which promoted the exposure of catalytic sites and facilitated the carrier separation and transfer. More importantly, the application of a light field significantly improved electron transport efficiency and enhanced the selectivity toward H<sub>2</sub>O<sub>2</sub> production by the 2e<sup>-</sup>ORR pathway. This work provides an important platform for developing high-performance carbon-based nanocomposites as metal-free photo-coupled electrocatalysts for the 2e<sup>-</sup>ORR to produce H<sub>2</sub>O<sub>2</sub>, which may offer more opportunities for industrial applications.

## DECLARATIONS

### Acknowledgments

This paper would like to acknowledge the teachers from the Experimental Analysis Center of Shanghai Normal University, as well as the partners of our research group.

### Authors' contributions

Made substantial contributions to conception and design of the study and performed data analysis and interpretation: Zhu Q, Fan J, Li G

Performed data acquisition, as well as provided administrative, technical, and material support: Tao Y, Shang H, Xu J, Zhang D, Li H

#### Availability of data and materials

Not applicable.

#### Financial support and sponsorship

This work was supported by the National Natural Science Foundation of China (Grant No. 21876113, 22176127, 22022608, and 21261140333) and the Singapore National Research Foundation under Grant No. NRF2017NRF-NSFC001-007. This work was also sponsored by Shanghai Rising-Star Program (No. 19QA1404100), Science and Technology Commission of Shanghai Municipality (No. 20ZR1421400) and Shanghai Engineering Research Center of Green Energy Chemical Engineering.

#### Conflicts of interest

All authors declared that there are no conflicts of interest.

#### Ethical approval and consent to participate

Not applicable.

#### Consent for publication

Not applicable.

#### Copyright

© The Author(s) 2022.

#### REFERENCES

1. Serra-maia R, Michel FM, Kang Y, Stach EA. Decomposition of hydrogen peroxide catalyzed by AuPd nanocatalysts during methane oxidation to methanol. *ACS Catal* 2020;10:5115-23. DOI
2. Chen H, Huang M, Yan W, Bai W, Wang X. Enzymatic regio- and enantioselective C-H oxyfunctionalization of fatty acids. *ACS Catal* 2021;11:10625-30. DOI
3. Teng Z, Yang N, Lv H, et al. Edge-functionalized g-C<sub>3</sub>N<sub>4</sub> nanosheets as a highly efficient metal-free photocatalyst for safe drinking water. *Chem* 2019;5:664-80. DOI
4. Hwang GB, Huang H, Wu G, et al. Photobactericidal activity activated by thiolated gold nanoclusters at low flux levels of white light. *Nat Commun* 2020;11:1207. DOI PubMed PMC
5. Cai J, Huang J, Wang S, et al. Crafting mussel-inspired metal nanoparticle-decorated ultrathin graphitic carbon nitride for the degradation of chemical pollutants and production of chemical resources. *Adv Mater* 2019;31:e1806314. DOI PubMed
6. Zhao H, Chen Y, Peng Q, Wang Q, Zhao G. Catalytic activity of MOF(2Fe/Co)/carbon aerogel for improving H<sub>2</sub>O<sub>2</sub> and OH generation in solar photo-electro-Fenton process. *Appl Catal B* 2017;203:127-37. DOI
7. Zong X, Chen H, Seger B, et al. Selective production of hydrogen peroxide and oxidation of hydrogen sulfide in an unbiased solar photoelectrochemical cell. *Energy Environ Sci* 2014;7:3347-51. DOI
8. Shi X, Zhang Y, Siahrostami S, Zheng X. Light-driven BiVO<sub>4</sub>-C fuel cell with simultaneous production of H<sub>2</sub>O<sub>2</sub>. *Adv Energy Mater* 2018;8:1801158. DOI
9. Mase K, Yoneda M, Yamada Y, Fukuzumi S. Seawater usable for production and consumption of hydrogen peroxide as a solar fuel. *Nat Commun* 2016;7:11470. DOI PubMed PMC
10. Liu N, Han M, Sun Y, et al. Ag-C<sub>3</sub>N<sub>4</sub> based photoelectrochemical cell using O<sub>2</sub>/H<sub>2</sub>O redox couples. *Energy Environ Sci* 2018;11:1841-7. DOI
11. Liu J, Zou Y, Jin B, Zhang K, Park JH. Hydrogen peroxide production from solar water oxidation. *ACS Energy Lett* 2019;4:3018-27. DOI
12. Campos-Martin JM, Blanco-Brieva G, Fierro JL. Hydrogen peroxide synthesis: an outlook beyond the anthraquinone process. *Angew Chem Int Ed Engl* 2006;45:6962-84. DOI PubMed
13. Kim HW, Bukas VJ, Park H, et al. Mechanisms of two-electron and four-electron electrochemical oxygen reduction reactions at nitrogen-doped reduced graphene oxide. *ACS Catal* 2020;10:852-63. DOI
14. Zhang T, Sun L, Sun X, Dong H, Yu H, Yu H. Radical and non-radical cooperative degradation in metal-free electro-Fenton based on

- nitrogen self-doped biochar. *J Hazard Mater* 2022;435:129063. DOI PubMed
15. He C, Sankarasubramanian S, Ells A, et al. Self-anchored platinum-decorated antimony-doped-tin oxide as a durable oxygen reduction electrocatalyst. *ACS Catal* 2021;11:7006-17. DOI
  16. Siahrostami S, Verdaguier-casadevall A, Karamad M, et al. Erratum: enabling direct H<sub>2</sub>O<sub>2</sub> production through rational electrocatalyst design. *Nature Mater* 2014;13:213-213. DOI
  17. Flaherty DW. Direct synthesis of H<sub>2</sub>O<sub>2</sub> from H<sub>2</sub> and O<sub>2</sub> on Pd catalysts: current understanding, outstanding questions, and research needs. *ACS Catal* 2018;8:1520-7. DOI
  18. Chen Y, Gao R, Ji S, et al. Atomic-level modulation of electronic density at cobalt single-atom sites derived from metal-organic frameworks: enhanced oxygen reduction performance. *Angew Chem Int Ed Engl* 2021;60:3212-21. DOI PubMed
  19. Melchionna M, Fornasiero P, Prato M. The rise of hydrogen peroxide as the main product by metal-free catalysis in oxygen reductions. *Adv Mater* 2019;31:e1802920. DOI PubMed
  20. Li BQ, Zhao CX, Liu JN, Zhang Q. Electrosynthesis of hydrogen peroxide synergistically catalyzed by atomic Co-N<sub>x</sub>-C sites and oxygen functional groups in noble-metal-free electrocatalysts. *Adv Mater* 2019;31:e1808173. DOI PubMed
  21. Jiang K, Back S, Akey AJ, et al. Highly selective oxygen reduction to hydrogen peroxide on transition metal single atom coordination. *Nat Commun* 2019;10:3997. DOI PubMed PMC
  22. Lu Z, Chen G, Siahrostami S, et al. High-efficiency oxygen reduction to hydrogen peroxide catalysed by oxidized carbon materials. *Nat Catal* 2018;1:156-62. DOI
  23. Lim JS, Kim JH, Woo J, et al. Designing highly active nanoporous carbon H<sub>2</sub>O<sub>2</sub> production electrocatalysts through active site identification. *Chem* 2021;7:3114-30. DOI
  24. Wang W, Tao Y, Fan J, et al. Fullerene-graphene acceptor drives ultrafast carrier dynamics for sustainable CdS photocatalytic hydrogen evolution. *Adv Funct Materials* 2022;32:2201357. DOI
  25. Dong K, Liang J, Wang Y, et al. Honeycomb carbon nanofibers: a superhydrophilic O<sub>2</sub>-entrapping electrocatalyst enables ultrahigh mass activity for the two-electron oxygen reduction reaction. *Angew Chem Int Ed Engl* 2021;60:10583-7. DOI PubMed
  26. San Roman D, Krishnamurthy D, Garg R, et al. Engineering three-dimensional (3D) out-of-plane graphene edge sites for highly selective two-electron oxygen reduction electrocatalysis. *ACS Catal* 2020;10:1993-2008. DOI
  27. Sun Y, Sinev I, Ju W, et al. Efficient electrochemical hydrogen peroxide production from molecular oxygen on nitrogen-doped mesoporous carbon catalysts. *ACS Catal* 2018;8:2844-56. DOI
  28. Wu Y, Gao Z, Feng Y, et al. Harnessing selective and durable electrosynthesis of H<sub>2</sub>O<sub>2</sub> over dual-defective yolk-shell carbon nanosphere toward on-site pollutant degradation. *Appl Catal B* 2021;298:120572. DOI
  29. Zhao X, Lei Y, Fang P, et al. Piezotronic effect of single/few-layers MoS<sub>2</sub> nanosheets composite with TiO<sub>2</sub> nanorod heterojunction. *Nano Energy* 2019;66:104168. DOI
  30. Zhang Y, Pan D, Tao Y, et al. Photoelectrocatalytic reduction of CO<sub>2</sub> to syngas via SnO<sub>x</sub>-enhanced Cu<sub>2</sub>O nanowires photocathodes. *Adv Funct Mater* 2022;32:2109600. DOI
  31. Yan J, Wang Y, Zhang Y, Xia S, Yu J, Ding B. Direct magnetic reinforcement of electrocatalytic ORR/OER with electromagnetic induction of magnetic catalysts. *Adv Mater* 2021;33:e2007525. DOI PubMed
  32. Yuan S, Li Y, Peng J, et al. Conversion of methane into liquid fuels-bridging thermal catalysis with electrocatalysis. *Adv Energy Mater* 2020;10:2002154. DOI
  33. Shen Q, Chen Z, Huang X, Liu M, Zhao G. High-yield and selective photoelectrocatalytic reduction of CO<sub>2</sub> to formate by metallic copper decorated Co<sub>3</sub>O<sub>4</sub> nanotube arrays. *Environ Sci Technol* 2015;49:5828-35. DOI PubMed
  34. Yang D, Yu H, He T, et al. Visible-light-switched electron transfer over single porphyrin-metal atom center for highly selective electroreduction of carbon dioxide. *Nat Commun* 2019;10:3844. DOI PubMed PMC
  35. Lu M, Zhang M, Liu CG, et al. Stable dioxin-linked metallophthalocyanine covalent organic frameworks (COFs) as photo-coupled electrocatalysts for CO<sub>2</sub> reduction. *Angew Chem Int Ed Engl* 2021;60:4864-71. DOI PubMed
  36. Yang H, Yang D, Zhou Y, Wang X. Polyoxometalate interlayered zinc-metallophthalocyanine molecular layer sandwich as photocoupled electrocatalytic CO<sub>2</sub> reduction catalyst. *J Am Chem Soc* 2021;143:13721-30. DOI PubMed
  37. Zhong H, Zhang Q, Wang J, et al. Engineering ultrathin C<sub>3</sub>N<sub>4</sub> quantum dots on graphene as a metal-free water reduction electrocatalyst. *ACS Catal* 2018;8:3965-70. DOI
  38. Chen Z, Zhao J, Cabrera CR, Chen Z. Computational screening of efficient single-atom catalysts based on graphitic carbon nitride (g-C<sub>3</sub>N<sub>4</sub>) for nitrogen electroreduction. *Small Methods* 2019;3:1800368. DOI
  39. Pei Z, Zhao J, Huang Y, et al. Toward enhanced activity of a graphitic carbon nitride-based electrocatalyst in oxygen reduction and hydrogen evolution reactions via atomic sulfur doping. *J Mater Chem A* 2016;4:12205-11. DOI
  40. Zhao X, Pan D, Chen X, et al. g-C<sub>3</sub>N<sub>4</sub> photoanode for photoelectrocatalytic synergistic pollutant degradation and hydrogen evolution. *Appl Surf Sci* 2019;467-468:658-65. DOI
  41. Kofuji Y, Isobe Y, Shiraishi Y, et al. Carbon nitride-aromatic diimide-graphene nanohybrids: metal-free photocatalysts for solar-to-hydrogen peroxide energy conversion with 0.2% efficiency. *J Am Chem Soc* 2016;138:10019-25. DOI PubMed
  42. Shiraishi Y, Kofuji Y, Sakamoto H, Tanaka S, Ichikawa S, Hirai T. Effects of surface defects on photocatalytic H<sub>2</sub>O<sub>2</sub> production by mesoporous graphitic carbon nitride under visible light irradiation. *ACS Catal* 2015;5:3058-66. DOI
  43. Chu C, Zhu Q, Pan Z, et al. Spatially separating redox centers on 2D carbon nitride with cobalt single atom for photocatalytic H<sub>2</sub>O<sub>2</sub> production. *Proc Natl Acad Sci USA* 2020;117:6376-82. DOI PubMed PMC

44. Liu Y, Li Q, Lian Z, et al. Polarization field promoted photoelectrocatalysis for synergistic environmental remediation and H<sub>2</sub> production. *Chem Eng J* 2022;437:135132. [DOI](#)
45. Zeng X, Liu Y, Kang Y, et al. Simultaneously tuning charge separation and oxygen reduction pathway on graphitic carbon nitride by polyethylenimine for boosted photocatalytic hydrogen peroxide production. *ACS Catal* 2020;10:3697-706. [DOI](#)
46. Hou H, Zeng X, Zhang X. Production of hydrogen peroxide by photocatalytic processes. *Angew Chem Int Ed Engl* 2020;59:17356-76. [DOI](#) [PubMed](#)
47. Desalegn BZ, Jadhav HS, Seo JG. Highly efficient g-C<sub>3</sub>N<sub>4</sub> nanorods with dual active sites as an electrocatalyst for the oxygen evolution reaction. *ChemCatChem* 2019;11:2870-8. [DOI](#)
48. Zhang P, Tong Y, Liu Y, et al. Heteroatom dopants promote two-electron O<sub>2</sub> reduction for photocatalytic production of H<sub>2</sub>O<sub>2</sub> on polymeric carbon nitride. *Angew Chem Int Ed Engl* 2020;59:16209-17. [DOI](#) [PubMed](#)
49. Wang H, Jia J, Song P, et al. Efficient electrocatalytic reduction of CO<sub>2</sub> by nitrogen-doped nanoporous carbon/carbon nanotube membranes: a step towards the electrochemical CO<sub>2</sub> refinery. *Angew Chem Int Ed Engl* 2017;56:7847-52. [DOI](#) [PubMed](#)
50. Wei Z, Liu M, Zhang Z, Yao W, Tan H, Zhu Y. Efficient visible-light-driven selective oxygen reduction to hydrogen peroxide by oxygen-enriched graphitic carbon nitride polymers. *Energy Environ Sci* 2018;11:2581-9. [DOI](#)
51. Dan R, Chen W, Xiao Z, et al. N-doped biomass carbon/reduced graphene oxide as a high-performance anode for sodium-ion batteries. *Energy Fuels* 2020;34:3923-30. [DOI](#)
52. Shen X, Xiao F, Zhao H, et al. In situ-formed PdFe nanoalloy and carbon defects in cathode for synergic reduction-oxidation of chlorinated pollutants in electro-fenton process. *Environ Sci Technol* 2020;54:4564-72. [DOI](#) [PubMed](#)
53. Zhang D, Liu T, Yin K, Liu C, Wei Y. Selective H<sub>2</sub>O<sub>2</sub> production on N-doped porous carbon from direct carbonization of metal organic frameworks for electro-Fenton mineralization of antibiotics. *Chem Eng J* 2020;383:123184. [DOI](#)
54. Watzel S, Hauenstein P, Liang Y, et al. Determination of electroactive surface area of Ni-, Co-, Fe-, and Ir-based oxide electrocatalysts. *ACS Catal* 2019;9:9222-30. [DOI](#)
55. Jakešová M, Apaydin DH, Sytnyk M, et al. Hydrogen-Bonded organic semiconductors as stable photoelectrocatalysts for efficient hydrogen peroxide photosynthesis. *Adv Funct Mater* 2016;26:5248-54. [DOI](#)
56. Wang M, Dong X, Meng Z, et al. An efficient interfacial synthesis of two-dimensional metal-organic framework nanosheets for electrochemical hydrogen peroxide production. *Angew Chem Int Ed Engl* 2021;60:11190-5. [DOI](#) [PubMed](#)
57. Hu J, Wang S, Yu J, Nie W, Sun J, Wang S. Duet Fe<sub>3</sub>C and FeNx sites for H<sub>2</sub>O<sub>2</sub> generation and activation toward enhanced electro-fenton performance in wastewater treatment. *Environ Sci Technol* 2021;55:1260-9. [DOI](#) [PubMed](#)
58. Wang W, Tao Y, Du L, et al. Femtosecond time-resolved spectroscopic observation of long-lived charge separation in bimetallic sulfide/g-C<sub>3</sub>N<sub>4</sub> for boosting photocatalytic H<sub>2</sub> evolution. *Appl Catal B* 2021;282:119568. [DOI](#)
59. McCrory CC, Jung S, Ferrer IM, Chatman SM, Peters JC, Jaramillo TF. Benchmarking hydrogen evolving reaction and oxygen evolving reaction electrocatalysts for solar water splitting devices. *J Am Chem Soc* 2015;137:4347-57. [DOI](#) [PubMed](#)